Multidimensional models for double-swept helicopter blades

Multidimensional Models for Double-Swept Helicopter Blades

Matteo Filippi [1], Enrico Zappino[2] and Erasmo Carrera[3]
Politecnico di Torino, Torino, To, 10129, Italy

This paper presents multidimensional finite element models for the analyses of modern helicopter blades. The methodology enables finite elements with different dimensionality to be joined together in a consistent fashion. The formulation exploits the unique feature of a special class of refined beam elements, which have pure displacements as unknowns. This property makes it possible to connect beam and solid elements at node levels without the need for complicated mathematical formulations. Various problems in the modelling of realistic blades can be tackled with ease such as the application of non-classical constraints. All physical surfaces of the structure can be modeled regardless of which finite element is utilized for discretizing the blade portion. Thus, three-dimensional stress states can be readily obtained by avoiding further post-processing operations. The multidimensional models have been verified with experimental results and validated with beam and shell finite element solutions available in the literature by considering tip-swept blades with rectangular cross-sections. The methodology has been then applied to a double-swept blade with a realistic profile.

---

[1] Research fellow PhD., Department of Mechanical and Aerospace Engineering, matteo.filippi@polito.it, MUL2 team http://www.mul2.polito.it
[2] Research fellow PhD., Department of Mechanical and Aerospace Engineering, enrico.zappino@polito.it, MUL2 team http://www.mul2.polito.it
[3] Full Professor of Aerospace Structures and Aeroelasticity, Department of Mechanical and Aerospace Engineering, erasmo.carrera@polito.it, MUL2 team http://www.mul2.polito.it

I. Introduction

Across the last 30 years, various research programmes, among others the British Experimental Rotor Programme - BERP, the Advanced Geometry Blade, the Advanced Technology Rotor, the *Etude d' un Rotor Aéroacoustique Technologiquement Optimisé* - ERATO, and the Blue-Edge blade, aimed at evaluating the effects of many parameters such as the tip shape, tapered profiles, and lamination schemes on both aerodynamic and structural characteristics of modern helicopter blades [1]. The test campaigns have motivated the development of new modelling techniques able to reproduce the experimental data numerically. Although the three-dimensional (3D) finite element (FE) approach would be the most reliable method, its use is often impracticable, especially during the preliminary design phase, when many stress, dynamic, and aerodynamic analyses must be carried out. Therefore, the need of a comprehensive and computationally efficient tool for the design activities justifies the idea of adopting models with smaller dimensionality than 3D models, namely the beam (or 1D) and plate/shell (or 2D) formulations [2].

Generally speaking, the 1D theories may be categorized according to which procedure is used to express the relations between the generalised stresses and strains above the cross-section [3]. The first category includes the axiomatic theories in which the primary variables are approximated using a certain number of cross-sectional coordinate functions to capture as many deformation mechanisms as possible [4, 5]. The axiomatic formulations are, therefore, implicitly based on some kinematic assumptions depending on the problem characteristics, e.g. the cross-section deformation modes, and the material properties. The second group of formulations aims at removing such hypotheses through rigorous cross-sectional analyses. One of the pioneering works is Ref. [6], where Giavotto *et al.* proposed a methodology for the calculation of stiffness and stresses of beams with arbitrary profiles, made of anisotropic and non-homogeneous materials. The procedure allowed the warping parameters and the global strains of central beam sections, *viz* not influenced by the end zones effects, to be determined by solving a 2D FE problem defined above the cross-section. The fully populated stiffness matrices computed with these analyses were then integrated into 1D formulations to perform global analyses of blade-like structures [7, 8]. Hodges and coworkers provided other remarkable contributions in this context with the development of the code VABS (Variational-

Asymptotical Beam Sectional Analysis) [9]. Based on the variational asymptotic method (VAM) proposed by Berdichevskii [10], the 3D problem is being split into two parts: the (mostly linear) cross-sectional analysis and the nonlinear, geometrically exact equations of motion along the longitudinal axis of the beam. The best set of sectional elastic constants, which are input parameters for the beam formulation, are obtained through an asymptotic analysis above the arbitrary-shaped cross-section [2]. The method enables three-dimensional displacement, stress, and strain fields to be recovered [11, 12] with a significant saving of computational cost. The VABS methodology has been included in many 1D codes such as the Rotorcraft Comprehensive Analysis System (RCAS) with the Generalized Composite Beam (GCB) element [13, 14] and the flexible multibody softwares DYMORE [15], and CAMRAD II [16].

Thanks to their accuracy and computational effectiveness, models using VABS-based 1D elements can be considered as the state-of-the-art in solving structural and aeroelastic problems for rotary-wing applications. The use of classical beam formulations, however, may reduce the applicability of such a sophisticated paradigm in some cases. Systematic comparisons with 3D [14] and 2D [17] FE solutions demonstrated that 1D results can differ to moderate, but not negligible, extent when highly-swept tip blades with a length-to-chord ratio lower than ten are evaluated. Furthermore, the need for simulating either realistic boundary conditions or nonuniform structures can exacerbate the limitations of these reduced techniques. For this reason, models joining both solid and shell formulations to 1D FE have been recently developed [17–19]. The connection of elements with different dimensionality may generate inconsistencies in the displacement and stress fields at the interface. Beam elements are usually based on classical kinematic models, e.g. the Timoshenko beam model, that cannot predict complex displacement fields. The link of these elements with three-dimensional FE requires the imposition of compatibility conditions to ensure the continuity of the displacement fields. To this end, multi-point constraints such as rigid body elements, transition elements, and variational coupling techniques have been conceived. Such methodologies provide satisfactory results in terms of global displacements and natural frequencies, but they may predict erroneous stress distributions at the interface level [20, 21].

This paper proposes a consistent methodology for joining 3D and 1D finite elements, which does not

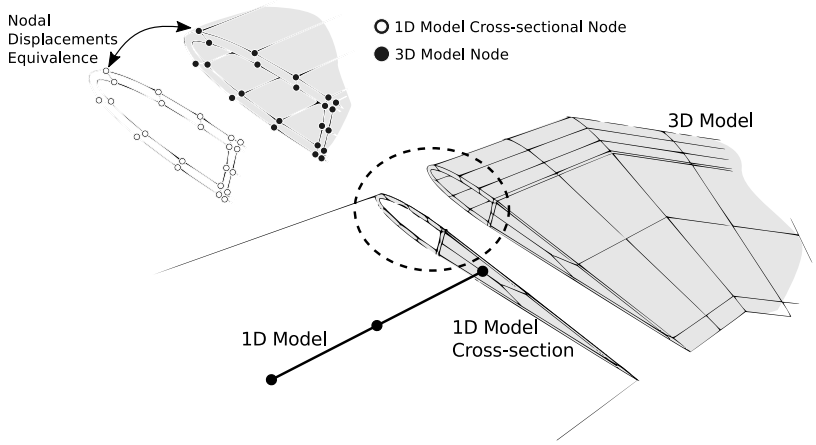

Fig. 1 Present variable kinematic model.

require either complicated mathematical manipulations or $ad-hoc$ assumptions. The procedure exploits the feature of a particular 1D kinematic formulation that uses only displacements as degrees of freedom. This property allows one to join directly the 1D and 3D elements by summing the elastic and inertial contributions of nodes shared by the two models. Figure 1 schematically illustrates the idea behind the procedure. The enhanced capabilities of the refined kinematic one-dimensional models make them able to predict complex cross-sectional deformations and, as a consequence, the coupling does not produce any stress concentration. The proposed multidimensional technique enables non-classical boundary conditions at the root blade to be imposed without the need of discretizing the region with 3D finite elements. The inherent three-dimensional nature of the 1D formulation allows one to model all physical surfaces of the structure and no post-processing procedure is required to recover the three-dimensional displacement, strain and stress fields. Both solid and beam finite elements are derived with ease by using a unified formulation.

II. Theoretical section

The multidimensional models are developed using the formalism of the Carrera Unified Formulation (CUF). CUF enables low- and high-fidelity structural theories to be generated automatically. The methodology is extensively used to conceive and compare different kinematic theories by going beyond the limitations of traditional 1D and 2D structural models, such as classical and first-order shear deformation theories. In this work, the indicial notation of CUF has also been adopted for

developing Lagrange-type solid elements in order to provide a comprehensive tool for generating multidimensional FE models. The following sections present the unified formulation for 1D and 3D finite elements, the equations of motion for rotating structures, and the assembling procedure.

Derivation of solid and beam finite elements via an unified formulation

According to the dimensionality of the considered finite element, the three-dimensional displacement field $\mathbf{u}(x, y, z, t) = (u_x\, u_y\, u_z)$ is being approximated as:

$$\begin{aligned} 3D - FE \longrightarrow \mathbf{u}(x,y,z,t) =& \mathbf{u}_{i\tau}(t) \cdot N_i(x,y,z) \cdot 1 && i = 1 \dots N_n^{3D} \\ 1D - FE \longrightarrow \mathbf{u}(x,y,z,t) =& \mathbf{u}_{i\tau}(t) \cdot N_i(y) \cdot F_\tau(x,z) \qquad \tau = 1 \dots M; && i = 1 \dots N_n^{1D} \end{aligned} \tag{1}$$

where N_i are the lagrangian 1D and 3D FE shape functions, F_τ are the functions used to approximate the solution above the beam cross-section ($x - z$ plane), and $\mathbf{u}_{i\tau}(t)$ is the vector of unknown coefficients. The index i refers to the finite element approximation and it ranges from 1 to the maximum number of elemental nodes, which is N_n^{3D} for the solid and N_n^{1D} for the beam element. The subscript τ is related to the expansion used for defining the cross-sectional kinematics and its maximum value, M, is an input parameter of the analysis. Although several functions F_τ can be utilized, the connection between 1D and 3D finite elements is particularly simple when Lagrange-type expansions (LE) are used. In this case, the beam kinematics is obtained as combinations of Lagrange polynomials that are defined within sub-regions (or elements) delimited by arbitrary numbers of points (or nodes). The number of points determines the order of the polynomial. Bi-linear (L4), bi-quadratic (L9), and bi-cubic expansions (L16) are obtained with four, nine and sixteen nodes, respectively. For the nine-point element (L9), the interpolation functions are

$$F_\tau = \tfrac{1}{4}(r^2 + r\, r_\tau)(s^2 + s\, s_\tau) \qquad \tau = 1, 3, 5, 7$$

$$F_\tau = \tfrac{1}{2}s_\tau^2(s^2 - s\, s_\tau)(1 - r^2) + \tfrac{1}{2}r_\tau^2(r^2 - r\, r_\tau)(1 - s^2) \qquad \tau = 2, 4, 6, 8 \tag{2}$$

$$F_\tau = (1 - r^2)(1 - s^2) \qquad \tau = 9$$

where r and s vary from -1 to $+1$, and r_τ and s_τ are the coordinates of the nine points in the natural coordinate system. The displacement field related to a 1L9 element is

$$\begin{aligned} u_x &= F_1\, u_{x_1} + F_2\, u_{x_2} + F_3\, u_{x_3} + ... + F_9\, u_{x_9} \\ u_y &= F_1\, u_{y_1} + F_2\, u_{y_2} + F_3\, u_{y_3} + ... + F_9\, u_{y_9} \\ u_z &= F_1\, u_{z_1} + F_2\, u_{z_2} + F_3\, u_{z_3} + ... + F_9\, u_{z_9} \end{aligned} \tag{3}$$

The unknowns $(u_{x_1}, ..., u_{z_9})$ have the same dimension and represent the translational displacements of the nine points of the element. Figure 2 shows a generic cross-section modelled using nineteen L9 elements (19L9).

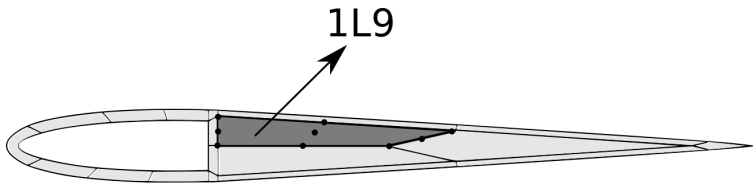

Fig. 2 Lagrange-type discretization of a generic cross-section.

For the 3D-FE (see Equation (1)), only the number of elemental nodes (N_n^{3D}) defines the type of the finite element, since all F_τ functions are equal to 1. In this case, tri-linear (HEXA-8) and tri-quadratic (HEXA-27) hexahedral elements are derived by using 8 and 27 nodes, respectively.

Governing Equations for rotating structures

The formulation is valid for small displacements, rotations, and amplitude vibrations, as well as for perfectly elastic materials. The assumption related to the geometrical linearity must be considered as a simplification of the problem rather than a limit of the theory. A fully 3D geometrical nonlinear formulation within the current framework was already presented and validated in Ref. [22] for dynamic analyses of rotating shell-like structures. Here, it has been assumed that the considered structures do not significantly deform under the action of the centrifugal loads. This hypothesis holds for many practical cases, even though it could be too restrictive when other loading conditions are considered (gravitational force at low rotational speeds). However, the stiffening contribution due to the centrifugal forces is taken into account by computing the linearized geometric stiffness

matrix.

The equations of motion are derived through the Principle of Virtual Work (PVW), which establishes the equilibrium condition between the virtual variations (denoted with δ) of works done by elastic deformations (δL_{int}), inertia (δL_{ine}) and external forces (δL_{ext})

$$\delta L_{int} = \delta L_{ine} + \delta L_{ext} \tag{4}$$

The strain energy can be written as:

$$\delta L_{int} = \int_V \delta\varepsilon^T \sigma \, dV \tag{5}$$

where ε and σ are the strain and stress vectors, respectively, and V is the initial volume of the body. By using Equation (1), the internal work becomes:

$$\delta L_{int} = \delta \mathbf{u}_{js}^T \underbrace{\left(\int_V F_s N_j \mathbf{b}^T \mathbf{C} \mathbf{b} N_i F_\tau dV \right)}_{\mathbf{K}^{ij\tau s}} \mathbf{u}_{i\tau} = \delta \mathbf{u}_{js}^T \mathbf{K}^{ij\tau s} \mathbf{u}_{i\tau} \tag{6}$$

The matrix $\mathbf{C}$ contains the coefficients of linear elastic materials and the matrix $\mathbf{b}$ is the linear differential operator that relates the three displacements to the strain components. It is possible to verify that $\mathbf{K}^{ij\tau s}$ is a 3-by-3 matrix for both solid and beam finite elements. The expressions of its terms do not depend either on the type and the number of functions used in the kinematic expansion. The global matrices are obtained by permuting the four indexes i, j, τ and s, regardless of which finite element is used. More details about the derivation of the fundamental nucleus can be found in Ref. [23].

The virtual work done by the inertial forces, $\mathbf{F}_I$, is

$$\delta L_{ine} = \int_V \delta \mathbf{u}^{\mathrm{T}} \mathbf{F}_I \, dV \tag{7}$$

Displacements and corresponding time derivatives, namely the velocities $\dot{\mathbf{u}}$ and accelerations $\ddot{\mathbf{u}}$, are expressed with respect to a coordinate reference frame attached to the blade that rotates at constant speed Ω. Accordingly, the inertial forces are

$$\mathbf{F}_I = -\rho \begin{pmatrix} \ddot{u}_x \\ \ddot{u}_y \\ \ddot{u}_z \end{pmatrix} - 2\,\rho\,\Omega \begin{pmatrix} -\dot{u}_y \\ \dot{u}_x \\ 0 \end{pmatrix} + \rho\,\Omega^2 \begin{pmatrix} u_x \\ u_y \\ 0 \end{pmatrix} + \rho\,\Omega^2 \begin{pmatrix} x_e \\ y_e \\ 0 \end{pmatrix} \tag{8}$$

The vector $\mathbf{r} = [x_e\, y_e, 0]$ defines the distance of a generic point with respect to the rotational axis. By substituting Equation (8) into Equation (7), the fundamental nuclei of the mass $\mathbf{M}^{ij\tau s}$, Coriolis $\mathbf{G}^{ij\tau s}$, centrifugal $\mathbf{K}_\Omega^{ij\tau s}$ matrices, and the centrifugal forces vector $\mathbf{F}_\Omega^{js}$ can be obtained with ease. On the other hand, the geometric stiffness matrix $\mathbf{K}_\sigma$ derives from the geometric strain energy defined as the product between the nonlinear part of strains, ε_{nl}, and the initial stress vector, σ_0. To compute the rotation-induced stresses, a static linear analysis is carried out

$$(\mathbf{K}_0 + \mathbf{K}_\Omega)|_{\Omega=1}\mathbf{u} = \mathbf{F}_\Omega|_{\Omega=1} \tag{9}$$

It should be underlined that the three-dimensional stress state is used to compute the geometric stiffness matrix, $\mathbf{K}_\sigma$. The natural frequencies (ω) and eigenvectors ($\bar{\mathbf{u}}$) associated with small-amplitude vibrations are obtained by assuming an harmonic solution ($\mathbf{u} = \bar{\mathbf{u}}\, e^{\sqrt{-1}\omega t}$) for the following homogeneous equation that is solved through the state-space transformation technique

$$\mathbf{M}\ddot{\mathbf{u}} + \mathbf{G}\dot{\mathbf{u}} + (\mathbf{K}_0 + \Omega^2\,\mathbf{K}_\sigma + \mathbf{K}_\Omega)\mathbf{u} = 0 \tag{10}$$

A. The assembling procedure: a simple example

The structural configuration of Fig. 3 is considered to explain the assembling procedure used. A prismatic structure has to be modeled with a beam and a solid element. The beam uses a 4-node Lagrange element (L4) over the cross-section and a two node beam element along the longitudinal axis. Figure 3 shows that the refined beam model has four nodes in each cross-section. The unknown displacements are, therefore, $\mathbf{u}_{i\tau}$=$(u_x\, u_y\, u_z)_{i\tau}$ with $i = 1, 2$ and $\tau = 1, 2, 3, 4$. On the other hand, the solid element has eight nodes in which the displacements have to be computed.

Since both models have the same unknowns, the imposition of compatibility between the shared

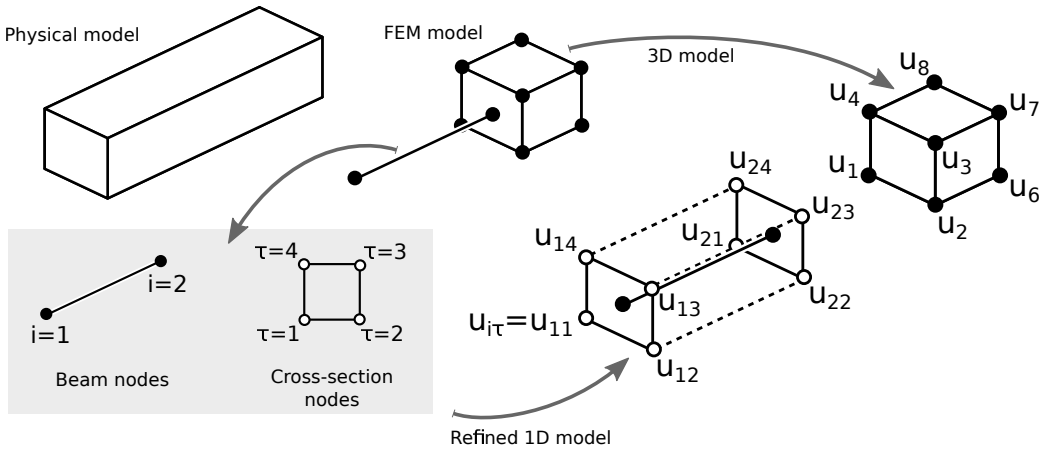

Fig. 3 Example of a multidimensional model: connection between a beam and a solid elements.

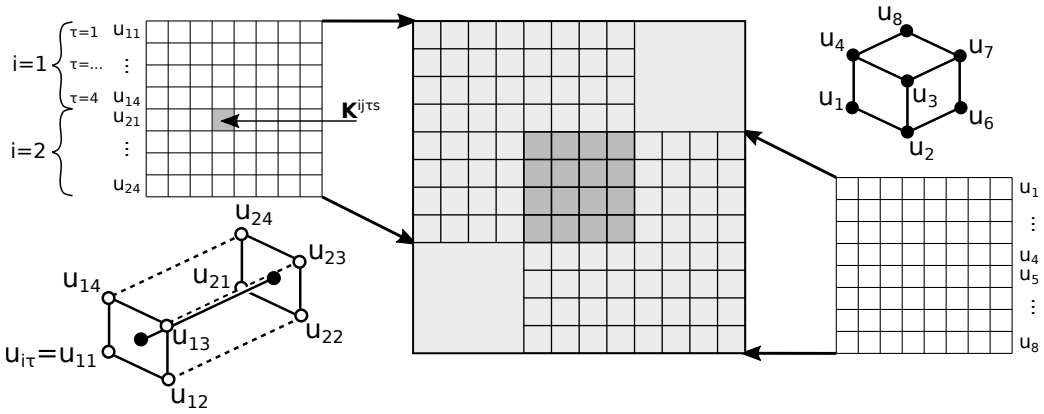

Fig. 4 Assembly of a multidimensional model where the elements have only displacements as unknowns.

nodes is straightforward:

$$\mathbf{u_{21} = u_1}, \qquad \mathbf{u_{22} = u_2}, \qquad \mathbf{u_{23} = u_3}, \qquad \mathbf{u_{24} = u_4}; \tag{11}$$

The conditions shown in Equation 11 can be used during the assembly procedure to identify the nodes that must be connected (see Fig. 4). The matrices of the two elements can be used to build the global matrix of the whole structure merely summing the contributions of the shared nodes. Since the assembled mathematical model has twelve structural nodes (SN), the degrees of freedom are 36 (DoF = SN $\times$ 3).

III. Numerical applications

A. Verification and Validation

To validate the current approach, the rotating swept-tip metallic blade shown in Fig. 5 was considered. The dimensions of the elastic portion were $L = 0.8001$ m, $s = 0.1524$ m, $t = 1.6002 \times 10^{-3}$ m, and $b = 2.54 \times 10^{-2}$ m, while, the length of the rigid hub was $r = 6.35 \times 10^{-2}$ m. The material properties taken from Ref. [24] were: Young' s modulus E =73.08 GPa, Poisson' s ratio $\nu = 0.325$, and density $\rho = 2682$ kg m^{-3}.

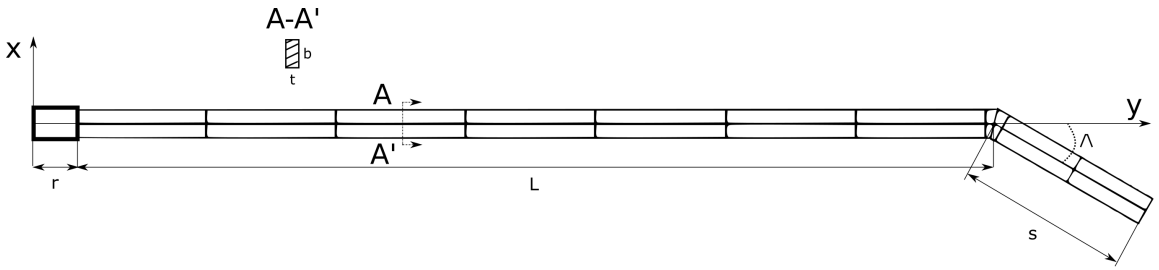

Fig. 5 Reference frame and geometry of the cantilever beam.

The mathematical model consisted of both 1D and 3D finite elements. The straight portion and the tip of the blade were discretized using, respectively, seven and two 4-node beam elements (B4), while, four 27-node hexahedral solid elements (HEXA-27) were utilized for the transition region. To ensure the connection between the 1D and 3D elements, two 9-node Lagrange elements (L9) were used to model the beam cross-section as shown in Fig. 6. The model had 1440 degrees of freedom.

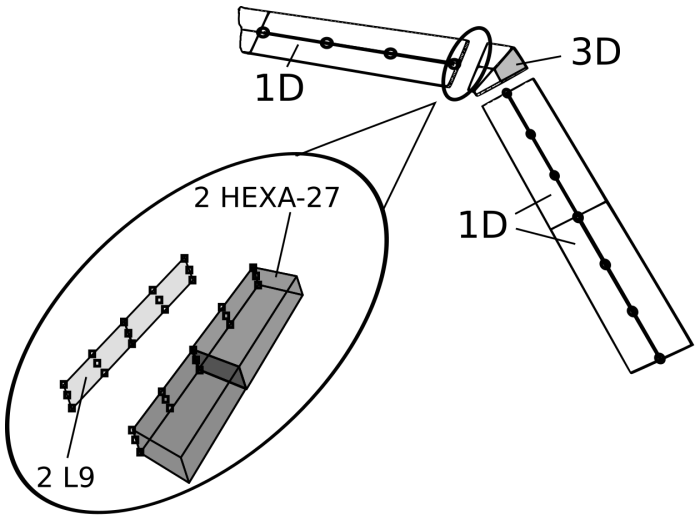

Fig. 6 Mathematical model for the swept-tip blade.

Figure 7 shows the frequencies computed at $\Omega = 750$ rpm for different sweep angles of the tip. The frequencies were related to mode shapes dominated by both flexural ('B') and torsional ('T') deformations. For comparison purposes, the experimental data ('Exp.') presented in Ref. [25] and the theoretical results obtained with a geometrically exact beam formulation ('NLB') developed in Ref. [24] have been reported. The comparisons revealed a good agreement between the three approaches, especially for mode shapes dominated by flexural deformations. For the torsional mode, some discrepancies between the NLB and the other two sets of results may be observed for the highest sweep angles.

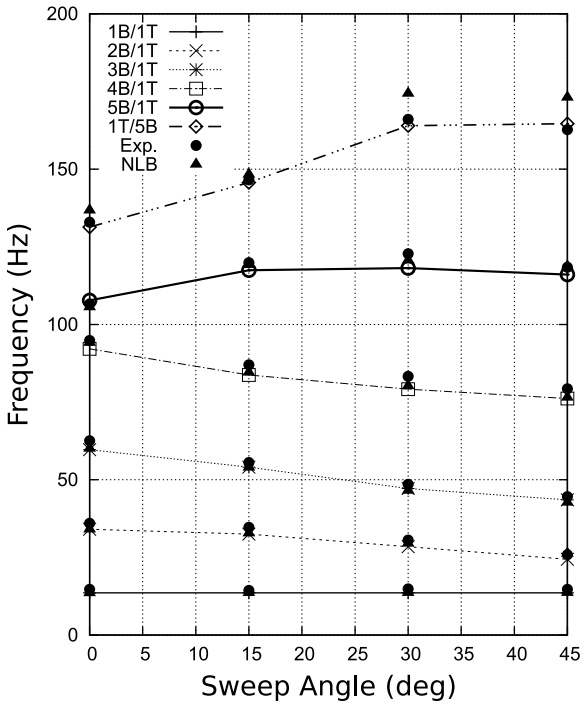

Fig. 7 Frequencies vs. tip sweep angle at 750 (rpm). 'B': bending mode, 'T': torsional mode.

On the other hand, the frequency variations with respect to the rotational speed are shown in Fig. 8 for $\Lambda = 45$ deg. Also for this case, the comparisons with experimental values of Ref. [25] at $\Omega =$ 0, 500, and 750 rpm have been provided.

In the second application, the hub radius, the straight portion, and the swept tip length were assumed to be equal to $r = 0.6985$, $L = 0.1651$, and $s = 0.1524$, respectively. The cross-section dimensions were not modified with respect to the previous example, while the following material properties were used: $E = 68.947$ GPa, $\nu = 0.3$, and $\rho = 2712$ kg m^{-3}. The outlined configuration

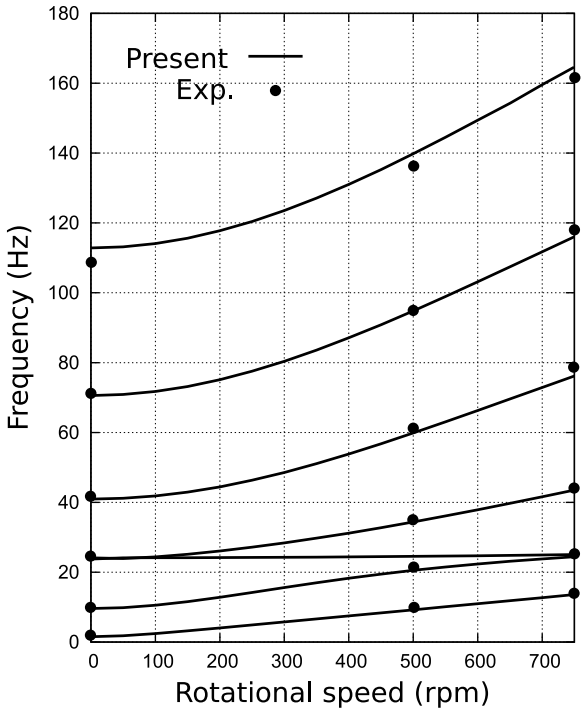

Fig. 8 Frequencies vs. Rotational speed for $\Lambda = 45$ (deg). Experimental data taken from Ref. [25].

was analyzed in Refs. [17] and [26] to compare the RCAS-GBC nonlinear 1D formulation with 2D and 3D solutions. The authors observed relevant discrepancies between the different approaches, especially for the highest sweep angles. The mathematical models depicted in Fig. 9 were utilized to investigate those mismatches.

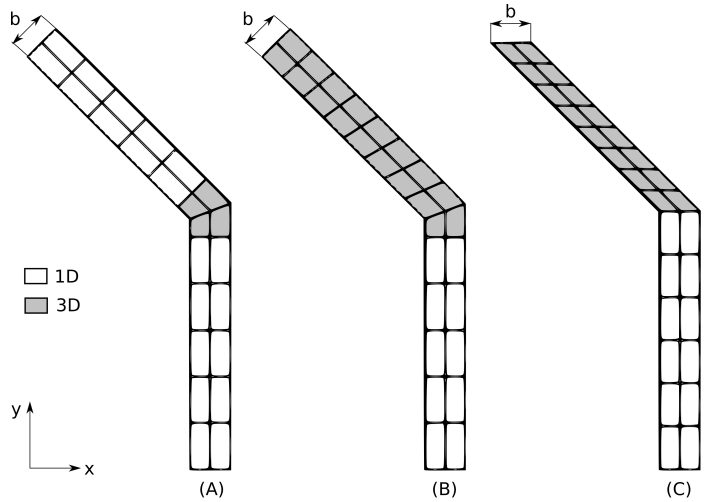

Fig. 9 Different mathematical models for the short swept-tip blade.

Model	F1	F2	F3	F4	F5	F6	DoF
2D FE solutions							
(1)	14.273	68.901	219.36	219.82	323.05	487.92	5346
(2)	16.533	71.319	223.94	248.10	367.11	571.66	5346
Present							
(A)	14.289	69.435	219.42	220.81	325.94	491.16	1575
(B)	14.335	69.439	220.02	220.02	327.06	492.23	1530
(C)	16.603	71.850	224.84	248.90	370.65	579.45	1575

Table 1 Natural frequencies (Hz) of swept-tip blades shown in Fig. 9.

In Model (A), the HEXA-27 elements were used for the transition region only, whereas in models (B) and (C), they were utilized for the whole swept portion. Although models (A) and (B) were different from each other, the structural geometry was approximated similarly. In these models, the chord was considered as the line perpendicular to the local longitudinal axes of both straight and swept portions. According to the model (C), the chord was considered parallel to the x-axis of the global reference system (see Fig. 5). It should be mentioned that model (C) corresponded to the discretizations adopted in Refs. [17] and [26]. Table 1 lists the natural frequencies at $\Omega = 0$ rpm computed with the current models. For verification purposes, two reference solutions obtained by using 800 4-node plate elements have also been reported. Solution (1) corresponded to the geometry of models (A) and (B), while solution (2) was related to the geometry of the model (C).

As expected, models (A) and (B) strongly agreed with the solution (1), while the model (C) provided almost the same results of the second reference solution. Figure 10 shows the Campbell's diagrams obtained with the three models. In particular, the results obtained with models (A) and (B) are shown in Fig. 10-a and compared with those derived by the beam formulation proposed in Ref. [17]. Figure 10-b compares, instead, the model (C) with 2D and 3D finite element solutions presented in Refs. [17] and [26], respectively. The comparisons revealed significant agreements with the reference solutions. Therefore, the relevant discrepancies observed between the Campbell's diagrams can be ascribed to the physical approximation of the geometry rather than to the dimensionality of the finite elements.

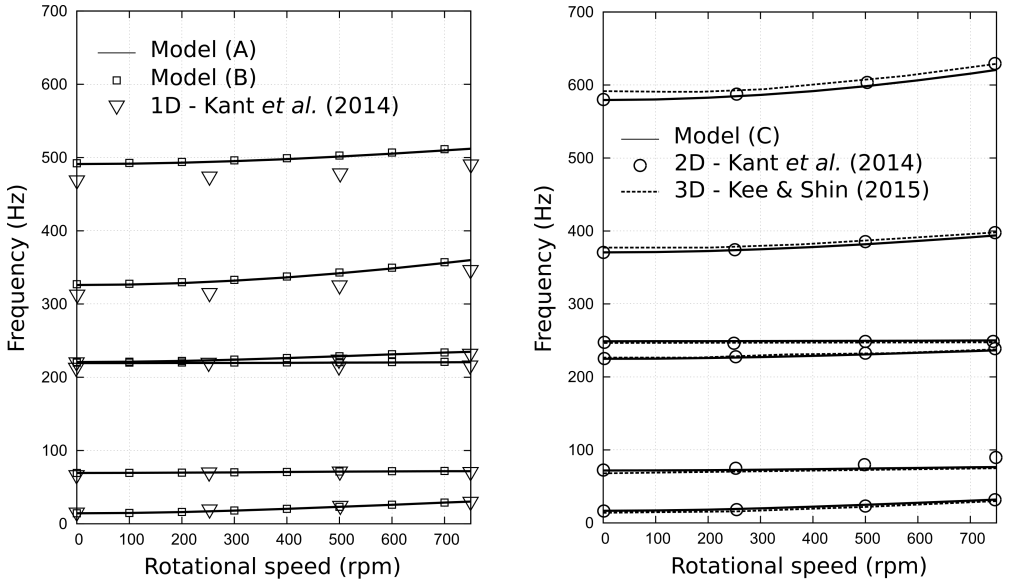

(a) (b)

Fig. 10 Frequencies vs. Rotational speed for the mathematical models of Fig. 9.

B. Double-swept rotor blade

The current methodology was used for the analysis of the double-swept blade configuration shown in Fig. 11. The dimensions cross-sectional profile was taken from Ref. [27]. The properties of the metallic skin (labeled with the subscript 'm') and of the foam ('f') were $E_m = 72.4$ Gpa, $\nu_m = 0.3$, $\rho_m = 2700$ kg m^{-3}, $E_f = 2.7$ Gpa, $\nu_f = 0.22$, and $\rho_f = 200$ kg m^{-3}. The length of the rigid hub was assumed to be equal to 1 m.

Table 2 reports the first ten natural frequencies at $\Omega = 0.0$ rpm computed with the mathematical models of Fig. 12 with the corresponding degrees of freedom. The last column lists the required time for the solution of each eigenvalues problem, by using a laptop with an Intel Core i7-5500U @ 2.40 GHz CPU. Models (A) and (B) combined 1D and 3D (HEXA-27) elements while the remaining ones consisted of solid elements only. Various discretizations were adopted for the two modeling approaches by changing the number of elements along the longitudinal axis and above the cross-section. As far as the multidimensional models (A) and (B) are concerned, four and eight 4-node beam elements have been used for discretizing the straight portions of the blade, respectively. For both models, the cross-section has been modeled by using nineteen L9 elements.

Even though mode shapes involved significant coupled deformations (see Fig. 13), the maximum

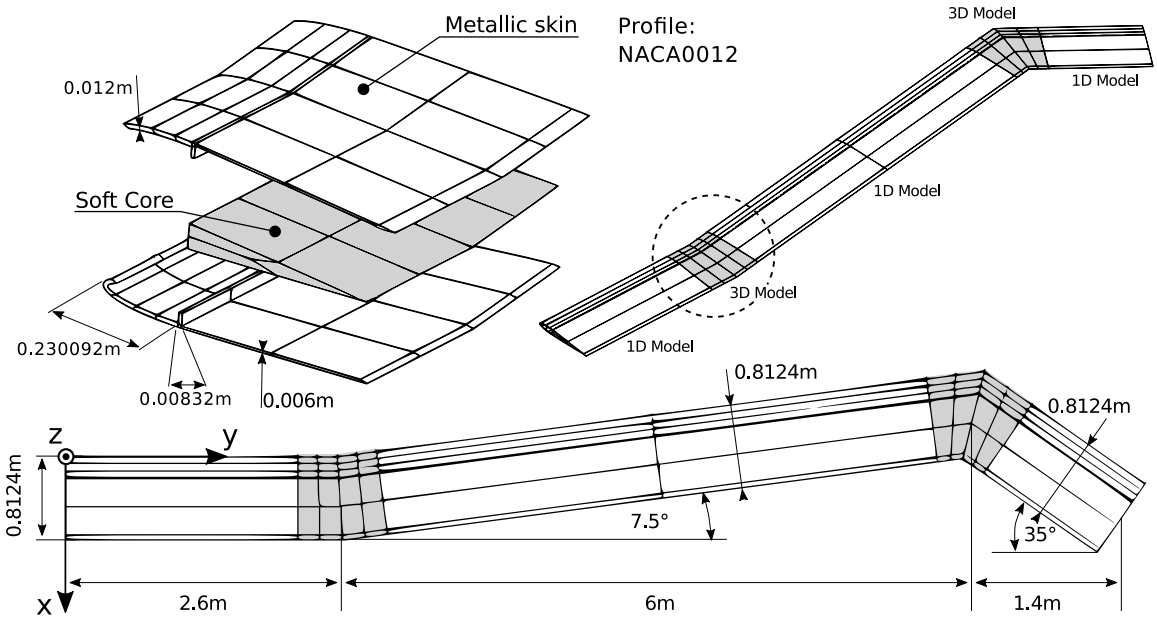

Fig. 11 Double-swept blade configuration.

Model	F1	F2	F3	F4	F5	F6	F7	F8	F9	F10	DoF	t (sec.)
(A)	0.654	4.142	5.977	9.102	15.42	24.72	36.77	37.36	46.21	58.46	8700	2.57
(B)	0.651	4.124	5.948	9.077	15.35	24.61	36.60	36.88	45.71	56.72	13200	5.15
3D-1	0.651	4.125	5.960	9.030	15.32	24.67	36.67	37.02	45.77	57.45	10500	3.54
3D-2	0.649	4.112	5.939	9.010	15.25	24.51	36.54	36.66	45.34	56.37	37500	18.29
3D-3	0.647	4.096	5.937	9.003	15.22	24.40	36.53	36.53	45.27	56.04	203808	107.93

Table 2 Natural frequencies (Hz) of the double-swept blade. The mathematical models are shown in Fig. 12.

discrepancy between the coarsest and the finest solution, namely models (A) and 3D-3, has been less than 5%.

The variations of the ten frequencies along with the rotational speed are shown in Fig. 14-a. It should be observed that the models predicted the same frequency changes up to 175 rpm. Beyond this threshold (see Fig. 14-b), slight discrepancies can be observed between Model (A) and the other numerical schemes in predicting the veering phenomenon of the second (F2) and fourth (F4) mode shape of Fig. 13. These mismatches can be ascribed to the FE mesh adopted in Model (A), which was not sufficient to provide convergent results.

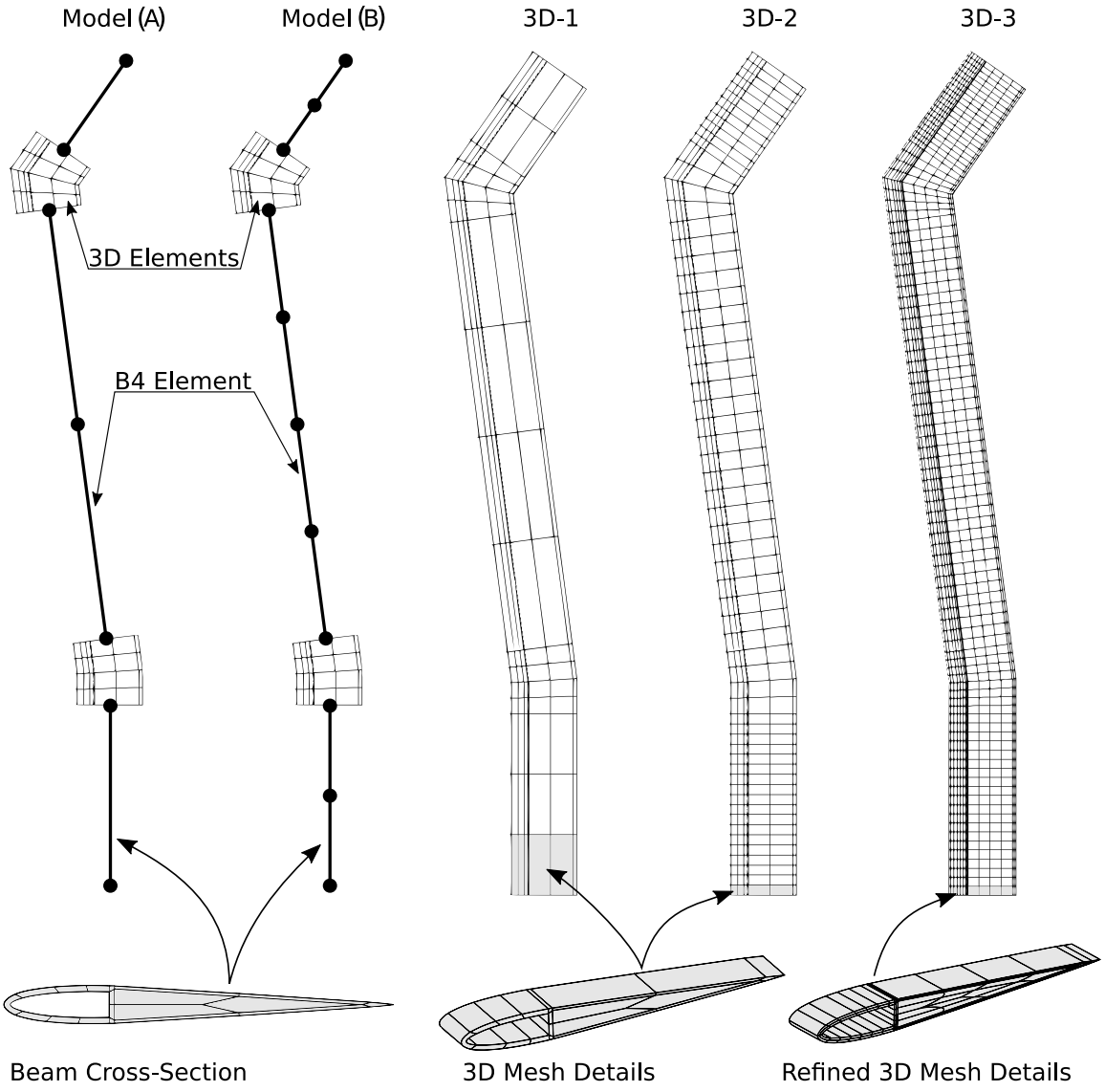

Fig. 12 Double-swept blade configuration.

IV. Conclusion

This paper presented dynamic analyses of blades with advanced geometries. The structures were modelled using finite elements of different dimensionality. In particular, 3D and 1D elements were connected with each other to reproduce all geometrical details of the blade. The connections were performed by exploiting the property of the Lagrange 1D kinematics, which has pure displacements as degrees of freedom. The use of advanced 1D formulations, wherever possible, enables the computational cost to be reduced by preserving a significant level of accuracy. The current methodology was validated using experimental data related to rotating swept-tip blades with a rectangular cross-

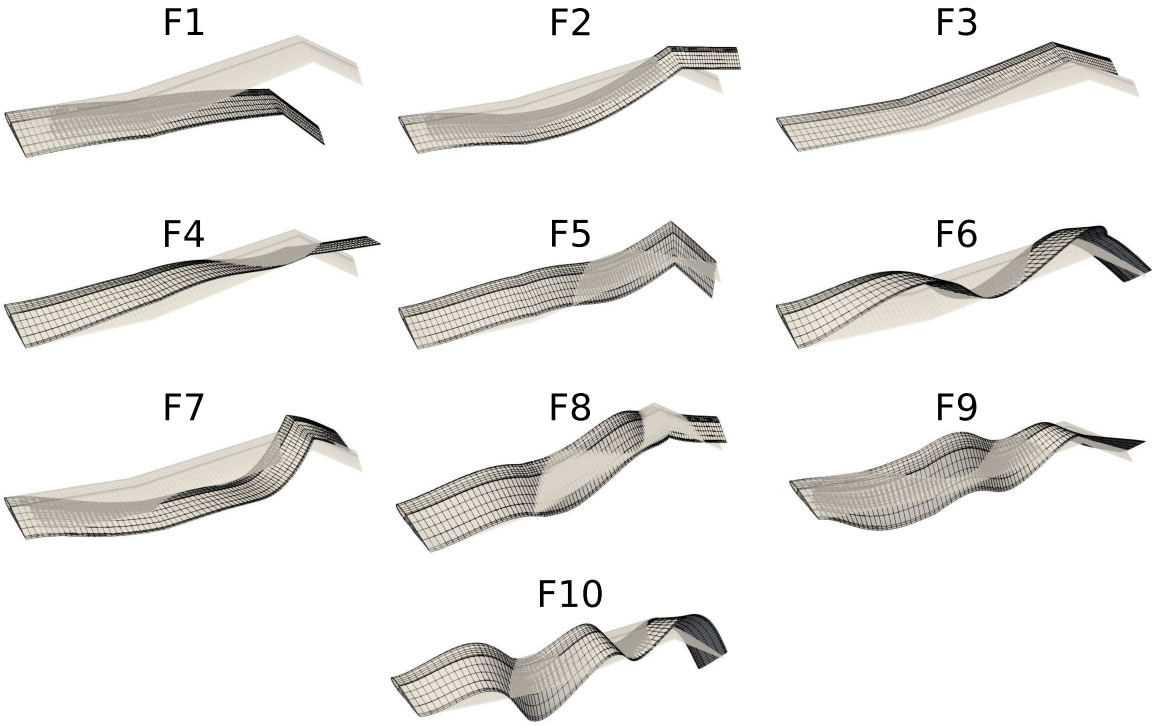

Fig. 13 Mode shapes obtained with the Model 3D-3.

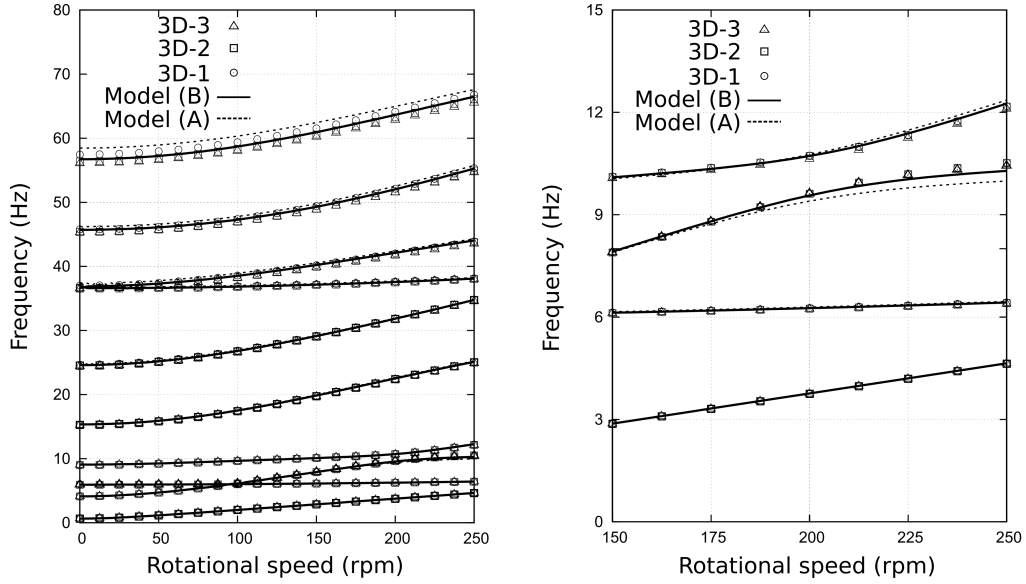

Fig. 14 Frequencies vs. Rotational speed for the double-swept blade.

section. Furthermore, the results were verified with numerical solutions obtained from nonlinear geometrical 1D and 2D formulations. Although the present methodology is linearized, the comparisons revealed a significant agreement with the reference solutions also for high sweep angles and

length-to-chord ratios. Eventually, both full-3D and 1D/3D models were utilized for analyzing the dynamics of a blade with a double-swept planform and a realistic cross-sectional profile. The results obtained with the convergent variable kinematic model accurately reproduced the full-3D solutions with a remarkable computational saving.

References

[1] Brocklehurst, A. and Barakos, G., "A review of helicopter rotor blade tip shapes," *Progress in Aerospace Sciences*, Vol. 56, 2013, pp. 35–74.

[2] Hodges, D. H., "Nonlinear Composite Beam Theory," 2006.

[3] Hodges, D. H., "Review of composite rotor blade modeling," *AIAA journal*, Vol. 28, No. 3, 1990, pp. 561–565.

[4] Song, O. and Librescu, L., "Structural Modeling and Free Vibration Analysis of Rotating Composite Thin-Walled Beams," *Journal of the American Helicopter Society*, Vol. 42, No. 4, 1997, pp. 358–369.

[5] Librescu, L. and Song, O., *Thin-walled composite beams: theory and application*, Vol. 131, Springer Science & Business Media, 2005.

[6] Giavotto, V., Borri, M., Mantegazza, P., Ghiringhelli, G., Carmaschi, V., Maffioli, G., and Mussi, F., "Anisotropic beam theory and applications," *Computers & Structures*, Vol. 16, No. 1-4, 1983, pp. 403–413.

[7] Borri, M. and Merlini, T., "A large displacement formulation for anisotropic beam analysis," *Meccanica*, Vol. 21, No. 1, 1986, pp. 30–37.

[8] Hodges, D. H., "A mixed variational formulation based on exact intrinsic equations for dynamics of moving beams," *International journal of solids and structures*, Vol. 26, No. 11, 1990, pp. 1253–1273.

[9] Hodges, D. H., Atilgan, A. R., Cesnik, C. E. S., and Fulton, M. V., "On a simplified strain energy function for geometrically nonlinear behaviour of anisotropic beams," Vol. 2, 1992, pp. 513–526.

[10] Berdichevskii, V., "Variational-asymptotic method of constructing a theory of shells: PMM vol. 43, no. 4, 1979, pp. 664–687," *Journal of Applied Mathematics and Mechanics*, Vol. 43, No. 4, 1979, pp. 711–736.

[11] Yu, W., Volovoi, V., Hodges, D. H., and Hong, X., "Validation of the variational asymptotic beam sectional analysis," Vol. 40, 2002, pp. 2105–2112.

[12] Yu, W., Hodges, D. H., and Ho, J. C., "Variational asymptotic beam sectional analysis âĂŞ An updated version," Vol. 59, 2012, pp. 40–64.

[13] Hodges, D. H., Saberi, H., and Ormiston, R. A., "Development of Nonlinear Beam Elements for Rotorcraft Comprehensive Analyses," Vol. 52, 2007, pp. 36–48.

[14] Truong, K.-V., Yeo, H., and Ormiston, R. A., "Structural dynamics modeling of rectangular rotor blades," Vol. 30, 2013, pp. 293–305.

[15] Bauchau, O. A. *DYMORE: User's Manual and Theory Manual.*.

[16] Johnson, W. "Rotorcraft Dynamics Models for a Comprehensive Analysis," *American Helicopter Society*

54th Annual Forum, Washington, DC, May 20âĂŞ22, 1998..

[17] Kang, H., Chang, C., Saberi, H., and Ormiston, R. A., "Assessment of beam and shell elements for modeling rotorcraft blades," *Journal of Aircraft*, Vol. 51, No. 2, 2014, pp. 520–531.

[18] Song, H. and Hodges, D., "Rigorous Joining of Advanced Reduced-Dimensional Beam Models to 2-D Finite Element Models," 2010.

[19] Hodges, D. H., "Unified Approach for Accurate and Efficient Modeling of Composite Rotor Blade Dynamics. The Alexander A. Nikolsky Honorary Lecture," Vol. 60, 2015, pp. 1–28.

[20] Carrera, E. and Zappino, E., "Carrera Unified Formulation for Free-Vibration Analysis of Aircraft Structures," *AIAA Journal*, Vol. 54, No. (1), 2016, pp. 280–292.

[21] Zappino, E. and Carrera, E., "Multidimensional Model for the Stress Analysis of Reinforced Shell Structures," *AIAA Journal*, Vol. 56, No. 4, 2017, pp. 1647–1661.

[22] Filippi, M., Pagani, A., and Carrera, E., "Accurate nonlinear dynamics and mode aberration of rotating blades," *Journal of Applied Mechanics*, 2018.

[23] Carrera, E., Cinefra, M., Petrolo, M., and Zappino, E., *Finite element analysis of structures through unified formulation*, John Wiley & Sons, 2014.

[24] Hodges, D. H., Shang, X., and Cesnik, C. E., "Finite element solution of nonlinear intrinsic equations for curved composite beams," *Journal of the American Helicopter Society*, Vol. 41, No. 4, 1996, pp. 313–321.

[25] Epps, J. J. and Chandra, R., "The natural frequencies of rotating composite beams with tip sweep," *Journal of the American Helicopter Society*, Vol. 41, No. 1, 1996, pp. 29–36.

[26] Kee, Y.-J. and Shin, S.-J., "Structural dynamic modeling for rotating blades using three dimensional finite elements," *Journal of Mechanical Science and Technology*, Vol. 29, No. 4, 2015, pp. 1607–1618, doi: 10.1007/s12206-015-0332-6.

[27] Jiang, F. and Yu, W., "Nonlinear variational asymptotic sectional analysis of hyperelastic beams," *AIAA Journal*, Vol. 54, No. 2, 2015, pp. 679–690.